Limitation of the Kirchhoff Boundary Conditions for Aerial Image Simulation in 157-nm Optical Lithography

Michael S. Yeung, *Member, IEEE,* and Eytan Barouch

***Abstract*—The aerial images of half-wavelength features with 0° and 180° phases obtained by using the Kirchhoff boundary conditions are compared with those obtained by using rigorous electromagnetic field computation for 248-nm lithography and 157-nm lithography. The discrepancies between the aerial images computed by the two methods are large at both wavelengths, but they are much larger for TM polarization at the wavelength $\lambda = 157$ nm. These discrepancies are due to diffraction effects in the aperture regions, which are more pronounced at $\lambda = 157$ nm because of the larger ratio of the thickness of the chromium absorber to the wavelength required at $\lambda = 157$ nm for a given attenuation factor. This shows that diffraction effects in the aperture regions must be included when simulating aerial images in 157-nm lithography.**

***Index Terms*—Aerial image simulation, Kirchhoff boundary conditions.**

I. Introduction

OPTICAL lithography is expected to be used for the manufacturing of integrated circuits through the 70-nm technology node employing ultraviolet light at the wavelength $\lambda = 157$ nm [1]. To assess the manufacturability of a 157-nm lithography process, one must have accurate knowledge of the aerial image intensity distribution as a function of optical system parameters such as numerical aperture and partial coherence.

The simplest approach to aerial image simulation is to employ the Kirchhoff boundary conditions [2] for the light passing through the mask apertures, in which diffraction in the aperture regions is neglected. This approach was shown to be inaccurate for aerial image simulation in extreme ultraviolet lithography (EUVL) at $\lambda \approx 13$ nm [3]–[5], due in part to the fact that the reflective masks used in EUVL have absorber thickness $d > 3\lambda$. Even in 248-nm lithography, in which transmission masks with absorber thickness $d < \lambda$ are used, discrepancies between the aerial images obtained from the Kirchhoff boundary conditions and those obtained from rigorous electromagnetic field computation have been reported [6]–[8].

The purpose of this letter is to show that, while transmission masks with $d < \lambda$ are also used in 157-nm lithography, the errors arising from the Kirchhoff boundary conditions are much larger in aerial image simulation at $\lambda = 157$ nm than at $\lambda = 248$ nm, for feature size below one wavelength and for TM polarization. This is due to the fact that the attenuation index κ of the chromium absorber in a mask at $\lambda = 157$ nm, namely, $\kappa = 1.11$, is smaller than its value of 2.01 at $\lambda = 248$ nm [9]. To achieve the same attenuation factor, the ratio d/λ at $\lambda = 157$ nm should be larger than the corresponding ratio at $\lambda = 248$ nm by a factor of $2.01/1.11$. This increase in d/λ leads to greater diffraction effects in the aperture regions at $\lambda = 157$ nm.

Manuscript received March 8, 2000; revised May 31, 2000. This work was supported by a MURI grant from AFOSR and DARPA. The review of this letter was arranged by Editor C.-P. Chang.

M. S. Yeung and E. Barouch are with the Department of Manufacturing Engineering, Boston University, Boston, MA 02215 USA (e-mail: myeung@bu.edu).

Publisher Item Identifier S 0741-3106(00)07255-4.

II. Simulation Method

To compute the electromagnetic fields in the vicinity of a mask aperture, the finite-difference time-domain (FDTD) method [10] is used. To simulate arbitrary angles of incidence in a partially coherent optical system, a special incident wave source is employed, in which the incident fields used to excite the computational domain are computed analytically by solving the FDTD equations for the layered, dispersive mask substrate [11]. The resulting incident fields are applied to all six sides of the computational domain. To obtain accurate FDTD results, a cell size corresponding to about 15 nodes per wavelength in the medium of largest refractive index is used.

To compute an aerial image, the fields in the vicinity of the mask aperture are propagated to the entrance pupil of the optical system in the far zone. In the FDTD case, the far-zone fields are obtained by integrating the FDTD fields over a closed surface enclosing the aperture, assumed to be isolated, using the dyadic Green's functions for the multilayered mask substrate [12], [13]. In the Kirchhoff case, the Kirchhoff fields in the aperture area are first obtained by doing an FDTD calculation without the chromium layer. The far-zone fields are then obtained by integrating the Kirchhoff fields over the aperture area using the free-space Green's function. The difference between computed FDTD and Kirchhoff diffracted fields is illustrated in Fig. 1 for a mask aperture with 180° phase.

III. Simulation Results

First, an alternating phase-shifting mask structure consisting of periodic lines and spaces of equal dimension W, with the phases of the spaces alternating between 0° and 180°, was simulated, to compare with the 248-nm results in the literature. Following [14], $d = 100$ nm and the refractive indices of chromium and quartz at 248 nm were assumed to be $n_{\text{chrome}} = 2.5 + 2.0j$ and $n_{\text{quartz}} = 1.51$. From the fields computed by FDTD, the

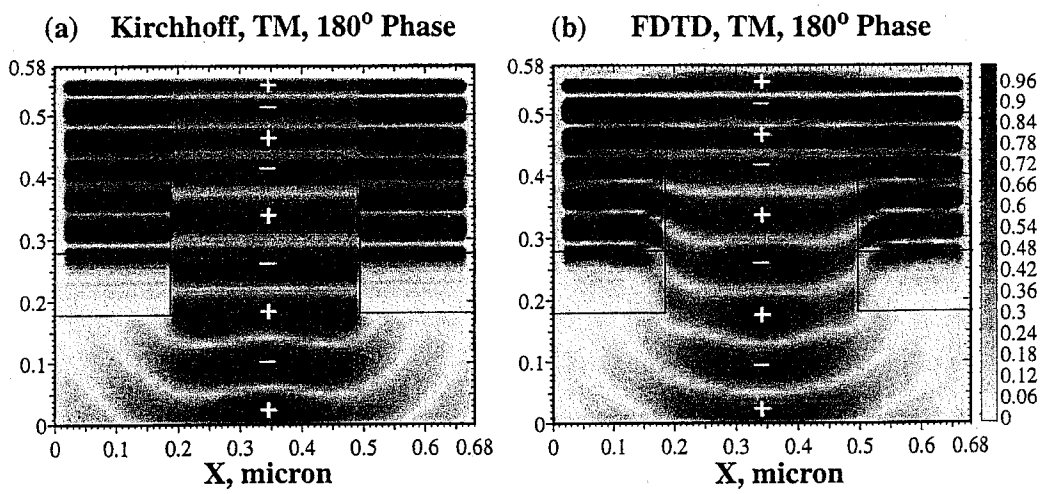

Fig. 1. Instantaneous magnitude of the electric field in the vicinity of a $2\lambda \times 12\lambda$ isolated mask aperture with 180° phase for a normally incident plane wave at $\lambda = 157$ nm with the electric vector polarized along the x-direction (TM). The plus and minus symbols denote the sign of the electric field. (a) Kirchhoff boundary conditions. (b) FDTD solution.

effective transmissions and phases (T_1, Φ_1) and (T_2, Φ_2) of the 0° and 180° phase regions, respectively, were extracted [14]. For $W = 1.0$ μm and TE polarization, in which the incident electric field is parallel to the lines and spaces, the results were $T_1 = 0.966, T_2 = 0.885$ and $\Phi_1 - \Phi_2 = 181.4°$. These are in good agreement with the results of [14], namely, $T_1 = 0.961, T_2 = 0.889$ and $\Phi_1 - \Phi_2 = 181.6°$.

Next, the above calculations were repeated for $W = 2\lambda$, corresponding to half-wavelength feature size in a 4X reduction system. For chromium, the refractive indices at $\lambda = 248$ nm and $\lambda = 157$ nm were taken from [9], namely, $n_{\text{chrome}} = 0.85 + 2.01j$ and $0.68 + 1.11j$, respectively. In both cases, a plasma permittivity function was needed to model the chromium [15]. The refractive indices of quartz at the two wavelengths were assumed to be $n_{\text{quartz}} = 1.51$ and 1.62, respectively. The thicknesses of the chromium at the two wavelengths were chosen to give similar attenuation factors, namely, $d = 100$ nm and $d = 115$ nm at $\lambda = 248$ nm and $\lambda = 157$ nm, respectively. The extracted effective transmissions and phase differences are shown in columns 2 to 4 of Table I. It can been seen that, whereas the effective transmissions for TE polarization at the two wavelengths are similar, those for TM polarization at 157 nm, namely, $(T_1, T_2) = (0.825, 0.699)$, are much smaller than the corresponding values at 248 nm, namely, $(T_1, T_2) = (0.934, 0.751)$. These large differences between the TE and TM results were only observed when a plasma model for the chromium was used.

Fig. 2 shows the average TM power densities P flowing through the 0° and 180° phase regions of the above mask structures. Here, $P = \int\int dx\, dy\, \text{Re}(\mathbf{E} \times \mathbf{H}^*) \cdot \mathbf{n}/(2A)$, where $(\mathbf{E}, \mathbf{H})$ are the electromagnetic fields, $\mathbf{n}$ is the unit vector in the negative z direction and A is the area of integration across the 0° or 180° phase region. It can be seen that the FDTD power density decreases much faster than the Kirchhoff power density as the wave propagates through the chromium layer containing the apertures. Furthermore, for the TM polarization shown, the decrease of the FDTD power density is much larger at $\lambda = 157$ nm than at $\lambda = 248$ nm. The ratios of the FDTD transmitted power density to the Kirchhoff transmitted power density for the 0° and 180° phase regions are shown in columns 5 and 6, respectively, of Table I. It can be seen that the values in columns 5 and 6 are roughly equal to the squares of the corresponding values in columns 2 and 3, respectively.

TABLE I
EFFECTIVE TRANSMISSION, PHASE DIFFERENCE AND TRANSMITTED POWER DENSITY OF ALTERNATING PHASE-SHIFTING MASK WITH $W = 2\lambda$

λ, Polarization	T_1	T_2	$\Phi_1 - \Phi_2$	$\left(\frac{P_{FDTD}}{P_{Kirchhoff}}\right)_1$	$\left(\frac{P_{FDTD}}{P_{Kirchhoff}}\right)_2$
248 nm, TE	0.962	0.748	181.8°	0.953	0.676
248 nm, TM	0.934	0.751	179.6°	0.843	0.662
157 nm, TE	0.945	0.767	179.4°	0.954	0.694
157 nm, TM	0.825	0.699	182.3°	0.716	0.611

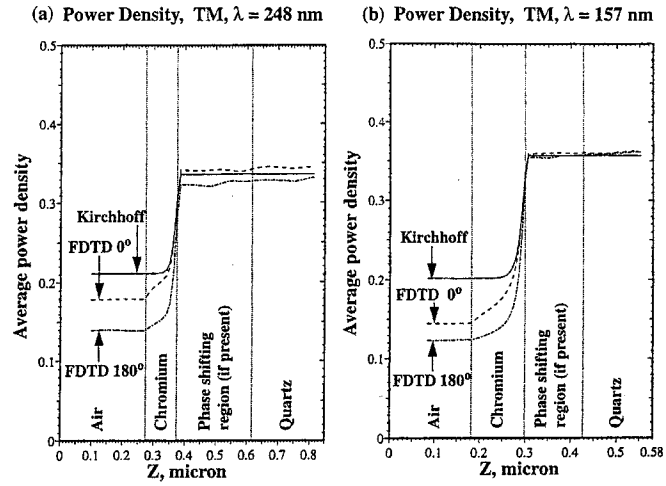

Fig. 2. Average TM power densities flowing through the 0° and 180° phase regions of an alternating phase-shifting mask structure with lines and spaces of equal dimension $W = 2\lambda$. (a) $\lambda = 248$ nm. (b) $\lambda = 157$ nm.

To simulate a partially coherent aerial image, the aerial images due to different source points on an extended incoherent

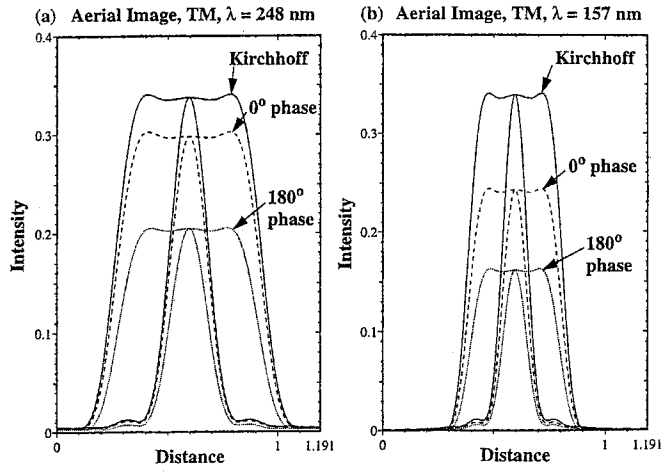

Fig. 3. Partially coherent aerial images of $2\lambda \times 12\lambda$ isolated mask apertures with 0° and 180° phases. The optical system parameters are NA $= 0.7$, $\sigma = 0.8$ and reduction ratio $= 4{:}1$. Each aerial image consists of two curves, corresponding to cross sections along the width and length of the image. The polarization is TM. (a) $\lambda = 248$ nm. (b) $\lambda = 157$ nm.

illuminator were computed separately and then averaged. An isolated $2\lambda \times 12\lambda$ mask aperture, corresponding to a $0.5\lambda \times 3\lambda$ feature on the wafer, was used. The computed partially coherent aerial images for 0° and 180° phases at zero defocus are shown in Fig. 3 for TM polarization. It can be seen that the ratios R of the FDTD center intensity to the Kirchhoff center intensity at $\lambda = 157$ nm, namely, $R = 0.716$ for 0° phase and $R = 0.476$ for 180° phase, are much smaller than the corresponding ratios at $\lambda = 248$ nm, namely, $R = 0.884$ for 0° phase and $R = 0.607$ for 180° phase. These results are consistent with the TM results in columns 5 and 6 of Table I.

IV. Conclusion

Diffraction effects in the aperture regions of 4X masks used for printing half-wavelength features at $\lambda = 248$ nm and $\lambda = 157$ nm have been compared with respect to three quantities obtained from FDTD computation, namely, effective transmission, transmitted power density and aerial image intensity. Results for the three quantities are consistent with each other. In particular, they show that the errors arising from the Kirchhoff boundary conditions in aerial image simulation are much larger at $\lambda = 157$ nm than at $\lambda = 248$ nm for TM polarization, when the chromium thicknesses at the two wavelengths are chosen to give similar attenuation factors.

References

[1] *National Technology Roadmap for Semiconductors*, Semiconductor Ind. Assoc., 1999.
[2] M. Born and E. Wolf, *Principles of Optics*, 5th ed. New York: Pergamon, 1975, p. 379.
[3] B. S. Bollepalli, M. Khan, and F. Cerrina, "Imaging properties of the extreme ultraviolet mask," *J. Vac. Sci. Technol. B*, vol. 16, pp. 3444–3448, 1998.
[4] ——, "Image formation in extreme ultraviolet lithography and numerical aperture effects," *J. Vac. Sci. Technol. B*, vol. 17, pp. 2992–2997, 1999.
[5] T. V. Pistor, K. Adam, and A. Neureuther, "Rigorous simulation of mask corner effects in extreme ultraviolet lithography," *J. Vac. Sci. Technol. B*, vol. 16, pp. 3449–3455, 1998.
[6] K. D. Lucas, A. J. Strojwas, K. K. Low, and C.-M. Yuan, "Intensity optimization for phase shifting masks," *Proc. SPIE*, vol. 1927, pp. 438–449, 1992.
[7] A. K. Wong and A. R. Neureuther, "Rigorous three-dimensional time-domain finite-difference electromagnetic simulation for photolithographic applications," *IEEE Trans. Semiconduct. Manufact.*, vol. 8, pp. 419–431, 1995.
[8] S. Tanaka, H. Nakamura, K. Kawano, and S. Inoue, "Practical topography design for alternating phase-shifting masks," *Proc. SPIE*, vol. 2726, pp. 473–484, 1996.
[9] E. D. Palik, Ed., *Handbook of Optical Constants of Solids II*. New York: Academic, 1991, pp. 374–385.
[10] A. Taflove, *Computational Electrodynamics: The Finite-Difference Time-Domain Method*. Boston, MA: Artech House, 1995.
[11] M. S. Yeung, "Incident wave source for finite-difference time-domain computation of electromagnetic scattering for objects embedded in layered dispersive media," *J. Sci. Comput.*, vol. 14, pp. 121–145, 1999.
[12] K. A. Michalski and J. R. Mosig, "Multilayered media Green's functions in integral equation formulation," *IEEE Trans. Antennas Propagat.*, vol. 45, pp. 508–519, 1997.
[13] M. S. Yeung and E. Barouch, "Three-dimensional mask transmission simulation using a single integral equation method," *Proc. SPIE*, vol. 3334, pp. 704–713, 1998.
[14] R. A. Ferguson, A. K. Wong, T. A. Brunner, and L. W. Liebmann, "Pattern-dependent correction of mask topography effects for alternating phase-shifting masks," *Proc. SPIE*, vol. 2440, pp. 349–360, 1995.
[15] R. Luebbers, F. Hunsberger, K. S. Kunz, R. B. Standler, and M. Schneider, "A frequency-dependent finite-difference time-domain formulation for dispersive materials," *IEEE Trans. Electromagn. Compat.*, vol. 32, pp. 222–227, 1990.